Numerical soil under heavy vehicles

Viktor Wiberg[a], Martin Servin[a,*], Tomas Nordfjell[b]

[a] *UmeåUniversity, SE-90187, Umeå, Sweden*
[b] *Swedish University of Agricultural Sciences, SE-90183, Umeå, Sweden*

Abstract

This paper addresses the challenges of creating realistic models of soil for simulations of heavy vehicles on soft terrain. We modelled soils using the discrete element method with variable parameters for surface friction, normal cohesion and rolling resistance. To find out what type of soils can be represented, we measured the internal friction and bulk cohesion of over 100 different virtual samples. To test the model, we simulated rut formation from a heavy vehicle with different loads and soil strengths. We conclude that the relevant space of frictional and frictional-cohesive soils can be represented and that the model is applicable for simulation-based experiments with heavy vehicles on soft terrain.

Keywords: Discrete Element Modelling, Multibody Dynamics, Soft Soil, Heavy Vehicles, Rut Formation, Multipass

---

1. Introduction

Heavy vehicles on soft terrain are associated with negative environmental impact, high fuel consumption and low productivity in agriculture and forestry [1, 2]. The effects can be reduced with improved vehicle design, transmission control and smart route planning. The difficulty is that any new solution need to perform well on a broad spectrum of situations, not just on singular cases. Computer-based simulation offers the possibility to carry out a large amount of experiments under repeatable and controlled conditions. The alternative, doing extensive testing with physical prototypes on a large variety of terrains, is neither economically nor practically feasible. The simulation-oriented research in this area has so far focused primarily on vehicle performance and less on the effects on the terrain, e.g. rut formation and soil compaction. This article addresses the challenges of creating realistic simulation models of terrain in interaction with heavy vehicles.

Particle-based terrain models, using the discrete element method (DEM), is a promising and versatile option for representing soil in simulations that also include multibody systems [3, 4]. As with real materials, the bulk properties of a particle-based terrain model depend on the shape and size distribution of the particles, their microscopic contact properties, and the packing density. Different combinations of particle properties result in soil beds that behave either like a rigid, elastic or plastic solid. A particle-based soil model can deform, fracture and split into smaller parts, flow rapidly and exhibit mixing and segregation phenomena. On the downside, discrete element simulations are computationally intense. With current technology, it is not possible to use the true particle size and shape distribution in simulations with terrain comparable in size to a full vehicle. Therefore materials are typically modelled as composed by *pseudo-particles* [5] of size chosen as large as possible, but small enough to resolve important deformations. The pseudo-particle shape, elasticity, friction, cohesion and rolling resistance are considered as model parameters which can be calibrated to produce material beds with desired bulk-mechanical (or *macroscopic*) properties, e.g. cone index, internal friction and bulk cohesion. The identification and calibration of the pseudo-particle (or *microscopic*) model parameters is made through experiments that are carried out identically for both real and virtual soils. However, it is not clear that each relevant set of soil strength parameters has a matching set of pseudo-particle parameters. Neither is it known to what extent the pseudo-particle method is valid for predicting the response of the terrain from a heavy vehicle.

A valid model should be able to predict the rut depth from single and multipass scenarios. Rut formation is a complex phenomena which depends on the subsoil stress distribution from an applied load. In regions of critical stress, the material is deformed plastically by dilatant shear and compaction. Thus, realistic rut formation is a strong indication that these phenomena are captured by the model. Also, rutting has been studied extensively and provides a good reference for comparison with simulations.

To answer which soils can be represented using the pseudo-particle approach, we created more than 100 virtual soil samples with different microscopic model parameters. The bulk-mechanical properties of such *soil simulants* were examined and quantified in terms of the internal friction and cohesion. For a selection of soil simulants, cone penetrometer tests were performed to determine the cone

---

[*] Corresponding author
Email address: `martin.servin@umu.se` (Martin Servin)

index. To study rut formation, we simulated repeated passes with a heavy vehicle over terrain beds. The rut depth was measured and compared to empirical models developed from field measurements.

1.1. Related work

A review of common tyre-terrain interaction models are found in [6]. Most examples of using the discrete element method for studying tyre-terrain interaction are limited to two-dimensional analysis or light-weighted vehicles, such as planetary rovers. In [7] it was shown that DEM is significantly better at predicting wheel performance on granular terrain than traditional Bekker-type terramechanics methods, which is fast to compute but limited to steady-state and simplistic wheel geometries. To the best of our knowledge, there is but one previous study of wheel rutting and mobility of heavy vehicles using particle-based terrain modelling in three dimension [8]. That paper, by Recuero et al., demonstrates that particle-based terrain in combination with multibody dynamics is indeed a feasible and versatile combination of simulation models for the study of heavy vehicle and terrain interaction. The qualitative behaviour agrees well with established theory of terramechanics. The particle parameters were, however, not calibrated to any specific soil and the bulk-mechanical properties were not examined. The simulated rut formation and vehicle mobility can therefore not be compared quantitatively with any empirical models and experimental data.

A review of different approaches to measure and calibrate DEM parameters is provided in [9]. Obermayr et al. [10] considered pseudo-particle modelling of three different soil types and performed model parameter calibration using a triaxial test. The models where then validated for excavation.

2. Modelling

We assume that vehicles and mechanical devices can be modelled as rigid multibody systems (MBS) and the soil using the discrete element method (DEM). Traditionally, these models are combined using co-simulation. Instead, we used a unified framework based on discrete variational mechanics and nonsmooth dynamics [11, 12]. This choice was motivated by computational speed, numerical stability and avoidance of non-physical coupling parameters that need tuning.

2.1. Discrete mechanics with contacts

The state of a rigid multibody system with N_b bodies, N_j joints and actuators and N_c contacts is represented on descriptor form in terms of the system position, $\boldsymbol{x}(t) \in \mathbb{R}^{6N_\mathrm{b}}$, velocity, $\boldsymbol{v}(t) \in \mathbb{R}^{6N_\mathrm{b}}$, and Lagrange multipliers, $\boldsymbol{\lambda}_\mathrm{j}(t) \in \mathbb{R}^{6N_\mathrm{j}}$ and $\boldsymbol{\lambda}_\mathrm{c}(t) \in \mathbb{R}^{6N_\mathrm{c}}$, that are responsible for the constraint forces due to the joints and contacts. The position variable is a concatenation of the spatial and rotational coordinates of the N_b bodies, $\boldsymbol{x} = [\mathbf{x}, \mathbf{e}]$, and the velocity vector holds the linear and angular velocities, $\boldsymbol{v} = [\mathbf{v}, \boldsymbol{\omega}]$. The time evolution of the multibody system state variables $[\boldsymbol{x}, \boldsymbol{v}, \boldsymbol{\lambda}]$ is given by the following set of equations

$$\boldsymbol{M}\dot{\boldsymbol{v}} = \boldsymbol{f}_\mathrm{ext} + \boldsymbol{G}_\mathrm{j}^\mathrm{T}\boldsymbol{\lambda}_\mathrm{j} + \boldsymbol{G}_\mathrm{c}^\mathrm{T}\boldsymbol{\lambda}_\mathrm{c} \tag{1}$$

$$\varepsilon_\mathrm{j}\boldsymbol{\lambda}_\mathrm{j} + \eta_\mathrm{j}\boldsymbol{g}_\mathrm{j} + \tau_\mathrm{j}\boldsymbol{G}_\mathrm{j}\boldsymbol{v} = \boldsymbol{u}_\mathrm{j}, \tag{2}$$

$$\texttt{contact\_law}(\boldsymbol{v}, \boldsymbol{\lambda}_\mathrm{c}, \boldsymbol{g}_\mathrm{c}, \boldsymbol{G}_\mathrm{c}), \tag{3}$$

where $\boldsymbol{f}_\mathrm{ext}$ is the external force, which like the constraint forces, $\boldsymbol{G}_\mathrm{j}^\mathrm{T}\boldsymbol{\lambda}_\mathrm{j}$ and $\boldsymbol{G}_\mathrm{c}^\mathrm{T}\boldsymbol{\lambda}_\mathrm{c}$, have dimension $\mathbb{R}^{6N_\mathrm{b}}$ and is composed of linear force and torque. The system mass matrix is $\boldsymbol{M} \in \mathbb{R}^{6N_\mathrm{b}\times 6N_\mathrm{b}}$. Eq. (2) is a generic constraint equation. An ideal joint can be represented with $\varepsilon_\mathrm{j} = \tau_\mathrm{j} = \boldsymbol{u}_\mathrm{j} = 0$, in which case Eq. (2) express a holonomic constraint, $\boldsymbol{g}_\mathrm{j}(\boldsymbol{x}) = 0$. A linear or angular motor may be represented by a velocity constraint $\boldsymbol{G}_\mathrm{j}\boldsymbol{v} = \boldsymbol{u}_\mathrm{j}(t)$ with set speed $\boldsymbol{u}_\mathrm{j}(t)$, which follows by $\varepsilon_\mathrm{j} = \eta_\mathrm{j} = 0$ and $\tau_\mathrm{j} = 1$. In the general case, Eq. (2) models a joint with constraint function $\boldsymbol{g}_\mathrm{j}(\boldsymbol{x})$, Jacobian $\boldsymbol{G} = \partial\boldsymbol{g}/\partial\boldsymbol{x}$, joint compliance ε_j and viscous damping rate τ_j. The holonomic and nonholonomic constraints can be seen as the limit of a stiff potential, $\mathcal{U}_\varepsilon = \frac{1}{2\varepsilon}\boldsymbol{g}^T\boldsymbol{g}$, or a Rayleigh dissipation function, $\mathcal{R}_\tau = \frac{1}{2\tau}(\boldsymbol{G}\boldsymbol{v})^T\boldsymbol{G}\boldsymbol{v}$, respectively. This offers the possibility of mapping known models of viscoelasticity to the compliant constraints. Descriptor form means that no coordinate reduction is made. The system is represented explicitly with its full degrees of freedom, although the presence of constraints. This is necessary for allowing non-ideal joints and for dynamic contacts at arbitrary locations.

We use a semi-implicit discrete variational time-stepping algorithm, that is presented in Appendix A together with a description of the equation solver. Here, we simply represent this as a function Φ for advancing the system state at fixed time-step Δt from time t_i to $t_{i+1} = t_i + \Delta t$

$$[\boldsymbol{x}_{i+1}, \boldsymbol{v}_{i+1}, \boldsymbol{\lambda}_{i+1}] = \Phi\left(\boldsymbol{x}_i, \boldsymbol{v}_i, \Delta t, \boldsymbol{g}, \boldsymbol{G}, \boldsymbol{p}\right) \tag{4}$$

where $\boldsymbol{p}$ are the model parameters. The constraint functions and Jacobians are evaluated at every time-step, based on the present configuration of joints and contacts, computed by means of geometric collision detection. We furthermore consider the system to have *nonsmooth dynamics* [13]. That means that the velocity and Lagrange multipliers are allowed to be arbitrarily discontinuous to reflect instantaneous changes due to impacts, frictional stick-slip transitions or joints and actuators reaching set limits. This is unavoidable when using an implicit integration scheme because of the coupling between state variables trough the contact law Eq. (3). Normal contacts and Coulomb friction is introduced as simple inequality constraints and complementarity conditions.

As particle contact law between particles we use a model that includes cohesive viscoelastic normal contacts (n), tangential Coulomb friction (t) and rolling resistance (r).

These are formulated in terms of inequality and complementarity conditions. The resulting model can be seen as a time-implicit version of the conventional discrete element method (DEM) and is therefore referred to as nonsmooth DEM (NDEM) [14, 12]. We use the following conditions as `contact_law` for each contact:

$$0 \le \varepsilon_{\mathrm{n}}\lambda_{\mathrm{n}} + g_{\mathrm{n}} + \delta_{\mathrm{c}}\tau_{\mathrm{n}}\boldsymbol{G}_{\mathrm{n}}\boldsymbol{v} \perp \lambda_{\mathrm{n}} \ge 0 \tag{5}$$

$$\lambda_{\mathrm{n}} \le c_{\mathrm{p}}A_{\mathrm{p}}/|\boldsymbol{G}_{\mathrm{n}}^{\mathrm{T}}| \quad \text{if } -\delta_{\mathrm{c}} \le g_{\mathrm{n}} \le 0, \tag{6}$$

$$\gamma_{\mathrm{t}}\boldsymbol{\lambda}_{\mathrm{t}} + \boldsymbol{G}_{\mathrm{t}}\boldsymbol{v} = 0, \quad |\boldsymbol{\lambda}_{\mathrm{t}}| \le \mu_{\mathrm{t}}|\boldsymbol{G}_{\mathrm{n}}^{\mathrm{T}}\lambda_{\mathrm{n}}| \tag{7}$$

$$\gamma_{\mathrm{r}}\boldsymbol{\lambda}_{\mathrm{r}} + \boldsymbol{G}_{\mathrm{r}}\boldsymbol{v} = 0, \quad |\boldsymbol{\lambda}_{\mathrm{r}}| \le r\mu_{\mathrm{r}}|\boldsymbol{G}_{\mathrm{n}}^{\mathrm{T}}\lambda_{\mathrm{n}}|, \tag{8}$$

where g_{n} is a function of the contact overlap and the Jacobians, $\boldsymbol{G}_{\mathrm{n}}$, $\boldsymbol{G}_{\mathrm{t}}$ and $\boldsymbol{G}_{\mathrm{r}}$ govern the normal, tangent and rotational directions of the contact forces. The parameters ε_{n}, τ_{n}, γ_{t} in Eq. (5) control the contact compliance and damping, and δ_{c} is the so-called cohesive overlap. Setting them equal to zero means that no penetration should occur, $g_{\mathrm{n}}(\boldsymbol{x}) \ge 0$, and if so the normal force should be repulsive, $\lambda_{\mathrm{n}} \ge 0$. The symbol $\perp$ is short notation for that complementarity condition [15]. Eq. (6) regulates the cohesive force that is capped to $f_{\mathrm{c}}^{\max} = c_{\mathrm{p}}A_{\mathrm{p}}$ in the cohesive overlap region, $\delta_{\mathrm{c}} > 0$, with particle cohesion c_{p} and particle cross section are A_{p}. A recommended cohesive overlap is $\delta_{\mathrm{c}} = 0.025d$. Eq. (7) states that contacts should have zero slide velocity, $\boldsymbol{G}_{\mathrm{t}}\boldsymbol{v} = 0$, giving rise to a friction force bounded by the Coulomb friction law with friction coefficient μ_{t}. Similarly, Eq. (8) states that, as long as the constraint torque is no greater than the rolling resistance law, relative rotational motion of contacting bodies is constrained, $\boldsymbol{G}_{\mathrm{r}}\boldsymbol{v} = 0$. Here, μ_{r} is the rolling resistance coefficient and r is the particle radius. Each contact adds $\dim(\lambda_{\mathrm{n}}, \boldsymbol{\lambda}_{\mathrm{t}}, \boldsymbol{\lambda}_{\mathrm{r}}) = 6$ additional variables and equations to the system.

We map the normal contact law, Eq. (5), to the nonlinear Hertz-Mindlin contact model, which follows from the theory of linear elasticity [16]. In that model the normal force is split into an elastic spring force and a viscous damping force

$$\boldsymbol{f}_{\mathrm{n}} = k_{\mathrm{n}}\delta^{3/2}\boldsymbol{n} + k_{\mathrm{n}}c_{\mathrm{d}}\delta^{1/2}\dot{\delta}\boldsymbol{n}, \tag{9}$$

where $\delta(\boldsymbol{x})$ and $\dot{\delta}(\boldsymbol{x})$ is the contact overlap and penetration velocity of two contacting spherical particles. The spring stiffness and damping coefficients are

$$k_{\mathrm{n}} = \frac{E\sqrt{2d^*}}{3(1-\nu^2)}, \tag{10}$$

$$c_{\mathrm{d}} = \frac{4(1-\nu^2)(1-2\nu)\eta}{15E\nu^2}, \tag{11}$$

where E is the Young's modulus, ν is Poisson's ratio and η is the material viscosity constant. The effective diameter between two interacting spheres, a and b, with diameter d_a and d_b is $d^* = (d_a^{-1} + d_b^{-1})^{-1}$. The mapping to Eq. (5) is accomplished by $g_{\mathrm{n}} = \delta^{5/4}$, $\varepsilon_{\mathrm{n}} = 5/4k_{\mathrm{n}}$ and $\tau_{\mathrm{n}} = \max(5c_{\mathrm{d}}/4, 4.5\Delta t)$, where the clamping of the damping time is explained in Appendix A.

The particle shape is an important material parameter for granular matter and soil, and is known to affect the internal friction. It is, however, also associated with increased computational complexity in simulations. Both the number of contacts and the time for computing each contact point increases with more complex shapes. It has been shown, both theoretically and experimentally, that many effects of particle angularity can be modelled with spherical particles and rolling resistance, see for instance [17]. We chose this approach.

2.2. Soil simulants

Using discrete elements, a virtual analogue of real soil was represented as packed collection of spherical particles defined as a *soil simulant.* To assure that experiments were conducted with identical packing we used three *simulant templates*, one for the triaxial, cone pentrometer and rut depth test. The templates had different sizes but were prepared in the same way. Initially, particles were emitted inside a closed container with frictionless smooth rigid walls. We used a fixed particle size distribution of $d \in \{24, 34, 40\}$ mm, set to make up 20, 30 and 50 per cent by mass. To achieve a spatially uniform distribution the samples were compressed isotropically at zero particle cohesion c_{p}, friction μ_{t} and rolling resistance μ_{r}. We found that a pressure of 10 kPa resulted in a porosity $\varphi = 0.30$ at static equilibrium, at which point the state of the soil was saved, as a template, for later use.

During test, we started with a simulant template and then set the model parameters μ_{t}, μ_{r} and c_{p} to create different soil simulants. Although the simulants did not explicitly contain water, the effects of pore pressures and fluid flow can be viewed as contained in the model parameters[1]. Apart from μ_{t}, μ_{r} and c_{p}, model parameters were held fixed. Since our study was restricted to the quasistatic regime, the coefficient of restitution, $e = 0$, and particle mass density, $\rho_{\mathrm{p}} = 2000\ \mathrm{kg/m}^3$, were assumed to have insignificant effects. Because the particles were moderately stiff, $E_{\mathrm{p}} = 100$ MPa, $\nu_{\mathrm{p}} = 0.3$, the bulk elasticity of soil depended more on porosity and particle shape (or effective rolling resistance).

In Appendix B we demonstrate that the simulations are invariant of particle size.

3. Bulk properties of terrain simulants

To asses what type of material a simulant represents, we used bulk mechanical parameters cohesion c and internal friction ϕ, which are standard in terramechanic studies and for characterizing soils. These parameter are used to describe the failure of soils in the Mohr-Coulomb criterion $\tau_{\mathrm{f}} = c + \sigma_{\mathrm{n}} \tan\ \phi$. It states that the shear stress at failure

---

[1] An increase in water content typically lowers the inter-particle tangential friction while increasing the cohesion.

τ_f is a function of the normal stress σ_n acting on the failure plane.

Another measure of soil strength is the cone index (CI). The CI is a widely used indicator of soil bearing capacity with original purpose to provide mobility and trafficability assessment for military vehicles [18]. To determine the CI, a cone is pushed into the soil at constant rate while measuring penetration resistance, i.e. the resisting force per cone base area. The penetration resistance is averaged between two depths to get a single value called the CI. Today, the CI database is large and has been used to develop empirical models related to rut formations [19].

To determine the CI, c, and ϕ of soil simulants, we simulated two separate bulk tests: the in-situ cone penetrometer test [18] and a consolidated drained triaxial test [20].

3.1. The triaxial cell

The triaxial cell was modelled as box-shaped (Figure 1) with perfectly smooth rigid wall boundaries. The test was carried out under gravity free conditions and divided into two phases: the consolidation phase and the shear phase. During consolidation the sample was subject to the confining stress level $\sigma_1 = \sigma_2 = \sigma_3$, controlled by monitoring the boundary forces and effective areas of each side. The consolidation phase took place until the pressure on each boundary was approximately static. In the shear phase, the vertical walls were driven inward in a strain-controlled manner at 0.25 m/s, corresponding to an inertial number of $I \lesssim 0.0025$ in the quasistatic regime [21]. The major stress σ_1 was registered over time as the lateral walls were adjusted to maintain constant minor stresses until the axial strain reached 25%.

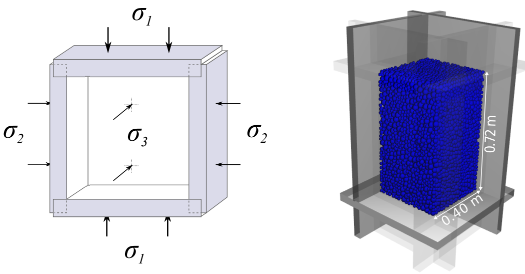

Figure 1: Illustration of the triaxial cell with plane side-walls (left) and a snapshot image of the simuation model (right).

To evaluate c and ϕ we fitted the Mohr-Coulomb failure criterion to the Mohr-circles drawn from $\sigma_2 = \sigma_3$ and peak strength. The peak strength was taken from simulation data as the largest deviator stress $\sigma_\mathrm{dev} = \sigma_1 - \sigma_3$.

3.2. The cone penetrometer

The cone penetrometer was modelled as a kinematic body consisting of two geometries, the sleeve cylinder and the cone, as shown in Figure 2. The cone had an apex angle of 30° in agreement with the original WES-cone and ASABE standard. Its diameter was chosen to be three times the mean particle diameter [22]. Particle-cone Young's modulus was set to 100 MPa, while μ_t and μ_r were assigned the inter-particle value and particle-cone cohesion and restitution, were set to zero.

After loading the *soil simulant template* and setting model parameters, the top boundary was removed and gravity introduced. It was verified that this action did not noticeably affect the soil porosity or configuration. The width of the template was chosen so that an increase in base sides showed insignificant effects on the resulting penetration resistance.

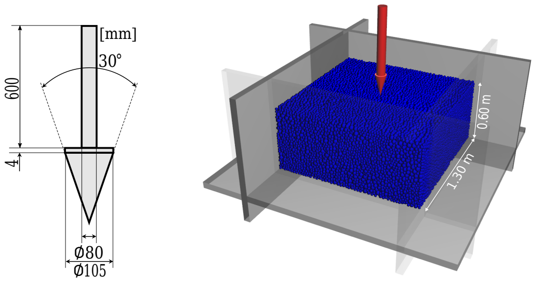

Figure 2: Cone penetrometer illustration (left) and corresponding simulation model (right).

During testing, the penetrometer was driven into the soil with a rate of 0.1 m/s [23], which corresponds to an inertial number of $I = 0.005$ in the quasistatic regime [21]. The penetration resistance was sampled until the cone tip reached a depth of 0.5 m. To find the CI, penetration resistance was averaged between 0.4-0.5 m.

3.3. Simulations

To investigate the space of numerical soils, we considered 100 combinations of model parameters in the range $c_\mathrm{p} \in [0, 50]$ kPa, $\mu_\mathrm{r} \in [0, 0.2]$, $\mu_\mathrm{t} \in [0, 0.7]$ generated using latin hypercube sampling with uniform distribution. For each sample we determined the stress parameters ϕ and c under $\sigma_2 = \sigma_3 \in \{30, 50\}$ kPa using the triaxial test.

To study the results of the triaxial test in further detail, we extended the original 100 samples with seven soils. Two of them were assigned zero inter-particle cohesion c_p, expected to be purely frictional, four were of different cohesive-frictional character and one was expected to be purely cohesive with zero μ_t and μ_r. To check if these soils obeyed the Mohr-Coulomb failure criterion, we included a supplementary confinement pressure of 100 kPa and plotted the three Mohr-circles together with the estimated linear envelope.

Finally, to see how the shear strength parameters were related to CI, we simulated the cone penetrometer test for each of the seven soils. In addition, we need the CI to compare simulated with predicted rut depths.

3.4. Results and discussion

The data of ϕ and c indicated that frictional and cohesive-frictional soils can be represented, while cohesive soils could not, as presented in Figure 3. A soil with high cohesion was only obtained with high inter-particle friction μ_t, leading to an increase in ϕ and resulting in a cohesive-frictional soil. As evident from Figure 3, μ_t was positively correlated with ϕ and c_p with c. However, the rolling resistance coefficient μ_r presented seemingly random behaviour. Data points with similar inter-particle friction and cohesion showed that an increase in rolling resistance leads to internal friction either increasing or remaining at the same level, but never decreasing. The bulk cohesion also tended to increase somewhat with an increase in rolling resistance. The reason why the relation is more clear, i.e. why there are many points in the middle figure with small internal friction despite large rolling resistance, can be explained by the saturation effect of the Coulomb friction law. When an individual contact is in sliding mode, this fact is not changed by an increase in rolling resistance. This phenomenon, and its effect on the bulk mechanical properties, have been studied thoroughly by Estrada et al. [24].

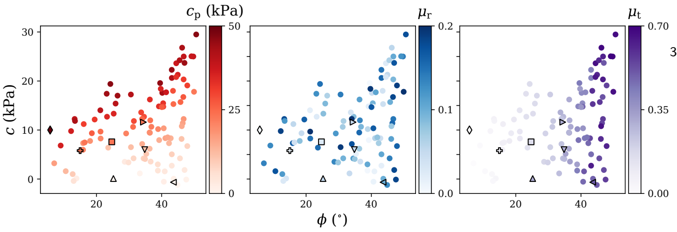

Figure 3: Soil strength parameter space (c, ϕ) using three difference colour maps, one for each model parameter $(c_\mathrm{p}, \mu_\mathrm{r}, \mu_\mathrm{t})$. Deviant markers refer to the complementary seven soils not part of the initial set of 100 samples, see Table 1.

The data from the seven complementary soils showed a variety in soil strength with a positive correlation between CI and the shear strength parameters, summarized in Table 1. As expected, two soils were frictional with near zero cohesion and four cohesive-frictional with non-zero cohesion and internal friction. However, the simulant expected to be cohesive, with no inter-particle friction and rolling resistance, resulted in an above zero internal friction (5.8 °) and only moderate cohesion (10 kPa). For a comparison with the original 100 soils, see the deviant markers in Figure 3.

Table 1: Pseudo-particle parameters and corresponding bulk mechanical properties of the seven complementary soils. Markers in left most column refer to Figure 3.

	Name	μ_t	μ_r	c_p (kPa)	ϕ (°)	c (kPa)	CI (kPa)
$<$	`fs_strong`	0.50	0.10	0.0	43.6	-0.65	950 ± 77
$\wedge$	`fs_weak`	0.30	0.05	0.0	25.2	0.10	400 ± 44
$>$	`cfs_strong`	0.30	0.05	23.4	34.4	11.6	1080 ± 105
$\vee$	`cfs_medium`	0.30	0.05	11.7	34.8	6.00	850 ± 51
□	`cfs_weak`	0.15	0.025	23.4	24.7	7.59	390 ± 21
+	`cfs_weakest`	0.06	0.01	23.4	15.0	5.80	160 ± 11
◊	`cs_weak`	0.00	0.00	50.0	5.8	10.0	120 ± 8

The stress-strain curves showed typical characteristics expected from real frictional and cohesive-frictional soils and the Mohr-circles drawn from the peak strengths formed linear envelopes. Figures 4 and 5 show stress-strain curves and Mohr-circles for three simulants: one frictional, one cohesive-frictional, and the soil which was expected to be cohesive. Dense frictional soils tend to have a distinct peak strength followed by a decrease in stress while the decrease in cohesive-frictional soils is less pronounced. This behaviour of real soils was observed for our soil simulants. In contrast, normally consolidated cohesive soils typically attain constant stress after failure and gain no strength with increasing confinement pressure. Therefore, we expected the curves in the upper right panel in Figure 4 to overlap, leading to Mohr-circles with identical radius in right panel of Figure 5. However, this is not the case and in line with our previous findings, that the particle-based approach is not capable of representing purely cohesive soils. We believe that the stress fluctuations from `cs_weak` (cf. upper right panel of Figure 4) are due to breakage of cohesive bonds, which causes rapid particle displacements. Although the fluctuations affect the peak strength, reducing them by using smaller particles would not result in equal radii Mohr-circles and a purely cohesive soil.

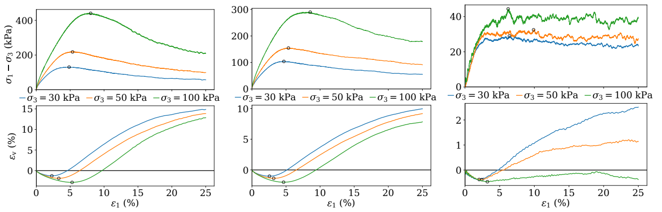

Figure 4: Deviator stress and volumetric strain as a function of axial strain for the soil simulants `fs_strong` (left), `cfs_medium` (middle) and `cs_weak` (right). The markers indicate the peak strength for each of the three confining pressures.

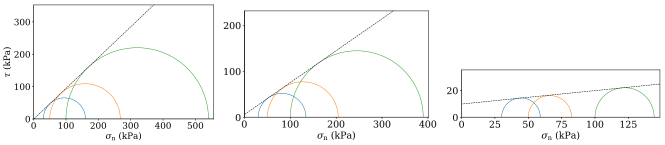

Figure 5: Mohr circles and the resulting Mohr-Coulomb failure envelope from the soil simulants `fs_strong` (left), `cfs_medium` (middle) and `cs_weak` (right).

The results of the cone penetrometer test showed that varying softness was represented by both frictional and cohesive-frictional soils, see Figure 6.

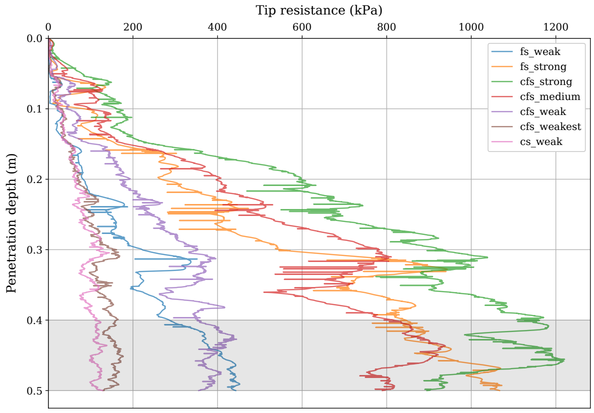

Figure 6: Curves from the cone penetrometer test for 7 different numerical soils. The CI is taken as the average tip resistance between 0.4 and 0.5 m depth (shaded region).

4. Rut depths

In this scenario, terrain simulants were exposed to a heavy vehicle where the resulting rut depth was measured after each one-lane pass. Rather than conducting new field experiments, we validated the particle-based terrain models by comparing simulated rut depths with empirical models: WES-based and multipass rut depth models.

4.1. WES-based rut depth models

To make rut depth predictions after the first vehicle pass we used the Waterways Experiment Station based rut depth models. The models rely on the CI as a measure of soil strength and combine it with tyre dimensions and wheel load into a empirical quantity called the *wheel numeric*. We used a numeric for tyres operating in cohesive-frictional soils

$$N_{\mathrm{cs}} = \frac{\mathrm{CI}\, b_{\mathrm{ty}}\, d_{\mathrm{ty}}}{W}, \tag{12}$$

where b_{ty} is the tyre width, d_{ty} is the diameter and W is the wheel load [25].

The N_{cs} numeric has been used as input in different WES-based rut depth models developed for various operating conditions. We considered two models by Anttila from data collected where an empty vehicle passes and then returns loaded over the same track [26]

$$z^{\mathrm{A}_1}_{\mathrm{rut}} = 0.005 + \frac{1.212}{N_{\mathrm{cs}}} \tag{13}$$

$$z^{\mathrm{A}_2}_{\mathrm{rut}} = \left(0.003 + \frac{0.910}{N_{\mathrm{cs}}}\right) d_{\mathrm{ty}}. \tag{14}$$

We also used a model by Saarilahti based on measurements carried out on a single track post vehicle pass [27],

$$z^{\mathrm{S}}_{\mathrm{rut}} = \frac{0.432}{N_{\mathrm{cs}}^{0.79}} d_{\mathrm{ty}}. \tag{15}$$

The rut depth models (13)-(15) should not normally be extrapolated to other conditions than those in which they were derived. However, independent studies have shown that these models may provide sufficient rut depth estimations [28]. Therefore, we consider it meaningful to compare empirically based predicted rut depths with simulated ones.

4.2. Multipass rut depth

To compare rut depth evolutions, we relied on the multipass sinkage model [29]

$$z_n = z_1 n^{\frac{1}{a}}, \tag{16}$$

which has also been successfully applied to rut depths. In such cases z_1 is the rut depth after the first wheel pass, $n > 1$ is any wheel pass and a is the multipass coefficient. The multipass coefficient can be determined by fitting rut depth data to model (16) using regression and typically lies between 2-3 for soft soil. Model (16) has also been used for full vehicles with rut depth measures after three or four wheels, depending on the vehicle, where observed values of a fall in the same range [28].

4.3. Quarter vehicle with two-wheeled bogie

The 3D vehicle model consisted of two main parts, the chassis and the two-wheeled bogie, constrained to move according to the illustrations in Figure 7. The purpose of the chassis was to mimic one quarter of the weight of a full eight-wheeled vehicle and could be adjusted depending on the load case. Each wheel had diameter $d = 1.5$ m and width $b = 0.65$ m and was driven by setting a fixed angular velocity. The tyres were treated as rigid, which is a reasonable model for pneumatic tyres with high inflation pressure on soft soil [18].

Regarding the tyre-particle contact parameters, any cohesion and restitution was set to zero and Young's modulus was assigned 100 GPa. The coefficient of friction was set to $\mu_{\mathrm{t}} = 0.6$ and the rolling resistance equal to the inter-particle value.

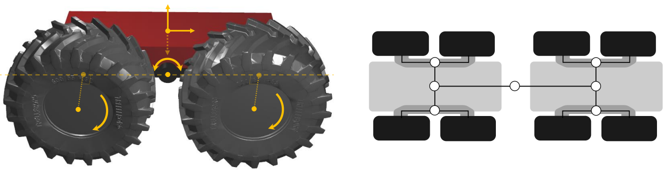

Figure 7: The 3D model of the quarter vehicle (left) and an illustration of a full vehicle (right). The arrows indicate unconstrained directions of motions.

4.4. Rut depth measurements

The vehicle was driven repeatedly over a flat elongated terrain with dimensions 6.5 × 1.3 × 0.6 m consisting of about 200 000 particles, see Figure 8. Before entering the terrain the vehicle was accelerated along an entry strip to its target velocity of 0.5 m/s. The vehicle then traversed the terrain to the point where the rear wheel reached an exit strip, at which the simulation state was saved and used as starting point for the next pass. The height of the entry and exit strips were then adjusted to the rut and the already accelerated vehicle was placed at the entry strip. This procedure was repeated for as many passes as desired. A sample video is available at `https://youtu.be/20jUWaTSo8A`.

The rut depths were computed at intervals of 0.04 m along a center patch of equal length as the quarter vehicle (3.22 m). In doing so, we avoided the areas closest to the entry and exit strips. The final rut depth from a single pass was taken as the average over the sectional depths.

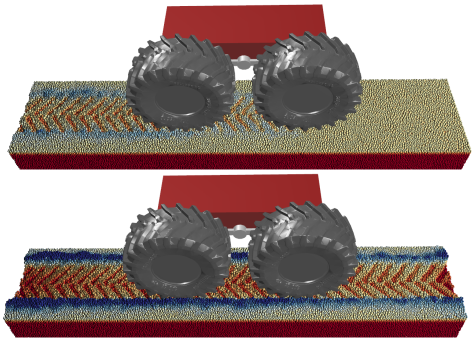

Figure 8: Sample images from a quarter vehicle-terrain simulation during the first (top) and third (bottom) pass. Particles have been colour coded by height, where the difference between deep blue and full red is 0.2 m. The entry and exit strips have been made transparent.

4.5. Simulations

We used the soil simulants **`cfs_weak`** and **`cfs_medium`** from Table 1 because they exhibit cohesive-frictional properties; typical for soils where rut formations are of concern. In addition, their CI indicates being of soft soil character, leading distinct rut formations from heavy vehicles.

To study the effect of different load cases on rut depth, three sets of simulations were conducted on the soil type **`cfs_weak`** using a vehicle mass of 3600, 4400 and 5200 kg. Our intention was to run ten subsequent passes for all load cases. However, due to the deep ruts caused by the heaviest vehicle, boundary effects became concerning and it was decided that only six passes be simulated. We also wanted to compare the rut depths between two soils of different bearing capacity (CI). Therefore, the stronger soil **`cfs_medium`** was tested by simulating ten passes with the 4400 kg vehicle.

For all four simulation sets, we calculated the predicted rut depths after the first vehicle pass from models (13)-(15). To find out if the multipass coefficient a lied in the expected range, we used non-linear regression to fit model (16) to the simulated rut depth evolutions.

4.6. Results

In all four cases, the simulated rut depths after the first vehicle pass were in good agreement with those of the empirical rut depth models (13)-(15), see Figure 9. Rut depth increased linearly with load, which is consistent with models (13) and (14). We also observed that a soil with higher CI led to a shallower rut.

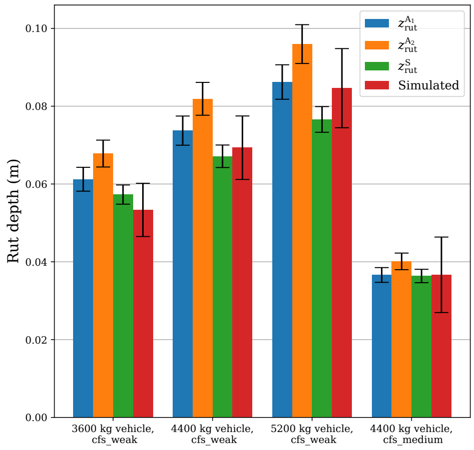

Figure 9: The predicted (blue, orange, green) and simulated (red) rut depths after the first vehicle pass, i.e. the second quarter vehicle. First three left groups are from different vehicle masses on the soil **`cfs_weak`** and the fourth group from **`cfs_medium`** and a vehicle mass of 4400 kg. Error bars correspond to one standard deviation.

The simulated rut depth evolutions showed that a stronger soil was less sensitive to repeated passes and soils became more sensitive when increasing the vehicle load, see Figure 10. The curves fitted to the data resulted in multipass coefficients within the expected range. In the case of the heaviest vehicle on **`cfs_weak`** it was below 2, which is reasonable considering the high load and soil softness. The other cases resulted in multipass coefficients between 2 and 3, which is consistent with empirical findings for soft soil.

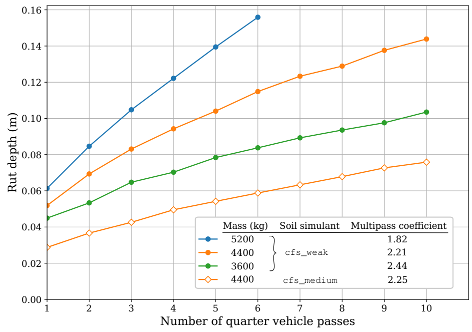

Figure 10: Rut depth evolutions on the soil **`cfs_weak`** using vehicle masses, 3600, 4400 and 5200 kg and on **`cfs_meadium`** using the 4400 kg vehicle. Only 6 quarter vehicle passes were simulated using the heaviest mass due to the deep resulting ruts.

5. Conclusion

We conclude that the particle-based terrain model can be used to study soil response from heavy vehicles. The relation between rut depth and the terrain's cone index, vehicle weight and tyre dimensions agree well with empirical observations. The terrain models are also capable of capturing the effect from repeated one-lane vehicle passes.

We characterize numerical soils in terms of cohesion and internal friction and show that frictional and cohesive-frictional soils of varying strength can be represented. To model purely cohesive soils, a possible solution is to extend or modify the inter-particle contact model, e.g. to use parallel bonds [30] or tangential cohesion [31]. The inability to represent purely cohesive soils does not lead to any significant limitations since the majority of trafficable soils are of cohesive-frictional character.

The present approach can enhance product development by running simulations of different vehicle designs on soils with known fundamental soil parameters. This also opens the possibility to study soil compaction and stresses under controlled and repeatable conditions in a way not possible during field experiments.

6. Acknowledgements

This work has in part been supported by Mistra Digital Forest (Grant DIA 2017/14 #6) and Skogtekniska Klustret AB and Algoryx Simulation AB. The simulations were performed on resources provided by the Swedish National Infrastructure for Computing (SNIC dnr 2019/3-168) at High Performance Computing Center North (HPC2N).

Appendix A. Numerical method

This appendix explain the numerical method for simulating the particle and multibody system.

The equaions of motion (1) and (2) form a set of differential algebraic equations (DAE) for the system variables $[\boldsymbol{x}, \boldsymbol{v}, \boldsymbol{\lambda}]$. DAEs are prone to numerical instability for many integration schemes. The theory of discrete variational mechanics offers a way to construct time-stepping algorithms with symmetry-preserving properties for mechanical systems. The key is to introduce discrete time already for the Lagrangian and action principle. The important symmetry properties, e.g. preservation of energy and momentum, can this way be built into the numerical scheme by design. The symplectic property of these integrators guarantee numerical stability and produce numerical solutions that shadow the exact trajectory with global bounds that depend on the time-step size. In many simulations of dynamical systems these properties are more important than high local resolution with an integrator that may diverge globally with time. SPOOK is a first order accurate discrete variational integrator [32], developed particularly for fixed time-step realtime simulation with non-ideal constraints like Eq. (1)-(2) and for contact laws like Eq. (5)-(8).

The SPOOK stepper is derived from a discrete variational formulation of nonholonomic and non-ideal constraints and has been proven linearly stable [32]. The numerical time integration scheme, $(\boldsymbol{x}_i, \boldsymbol{v}_i) \rightarrow (\boldsymbol{x}_{i+1}, \boldsymbol{v}_{i+1}, \boldsymbol{\lambda}_{i+1})$, for computing the position, velocity and Lagrange multiplier at time $t_{n+1} = t_n + \Delta t$ from previous state at time t_i involve solving the following mixed complementarity problem (MCP) [15]

$$\begin{gathered} \boldsymbol{H}\boldsymbol{z} + \mathbf{b} = \mathbf{w}_l - \mathbf{w}_u \\ 0 \leq \mathbf{z} - \mathbf{l} \perp \mathbf{w}_l \geq 0 \\ 0 \leq \mathbf{u} - \mathbf{z} \perp \mathbf{w}_u \geq 0 \end{gathered} \tag{A.1}$$

where

$$\boldsymbol{H} = \begin{bmatrix} \boldsymbol{M} & -\boldsymbol{G}_{\mathrm{n}}^{\mathrm{T}} & -\boldsymbol{G}_{\mathrm{t}}^{\mathrm{T}} & -\boldsymbol{G}_{\mathrm{r}}^{\mathrm{T}} & -\boldsymbol{G}_{\mathrm{j}}^{\mathrm{T}} \\ \boldsymbol{G}_{\mathrm{n}} & \boldsymbol{\Sigma}_{\mathrm{n}} & 0 & 0 & 0 \\ \boldsymbol{G}_{\mathrm{t}} & 0 & \boldsymbol{\Sigma}_{\mathrm{t}} & 0 & 0 \\ \boldsymbol{G}_{\mathrm{j}} & 0 & 0 & \boldsymbol{\Sigma}_{\mathrm{r}} & 0 \\ \boldsymbol{G}_{\mathrm{j}} & 0 & 0 & 0 & \boldsymbol{\Sigma}_{\mathrm{j}} \end{bmatrix}, \tag{A.2}$$

$$\boldsymbol{z} = \begin{bmatrix} \boldsymbol{v}_{n+1} \\ \boldsymbol{\lambda}_{\mathrm{n},n+1} \\ \boldsymbol{\lambda}_{\mathrm{t},n+1} \\ \boldsymbol{\lambda}_{\mathrm{r},n+1} \\ \boldsymbol{\lambda}_{\mathrm{j},n+1} \end{bmatrix}, \quad \boldsymbol{b} = \begin{bmatrix} -\boldsymbol{M}\boldsymbol{v}_n - \Delta t \boldsymbol{M}^{-1}\boldsymbol{f}_{\mathrm{ext}} \\ \frac{4}{\Delta t}\boldsymbol{\Upsilon}_{\mathrm{n}}\boldsymbol{g}_{\mathrm{n}} - \boldsymbol{\Upsilon}_{\mathrm{n}}\boldsymbol{G}_{\mathrm{n}}\boldsymbol{v}_n \\ 0 \\ 0 \\ -\boldsymbol{\omega}_{\mathrm{j}} + \frac{4}{\Delta t}\boldsymbol{\Upsilon}_{\mathrm{j}}\boldsymbol{g}_{\mathrm{j}} - \boldsymbol{\Upsilon}_{\mathrm{j}}\boldsymbol{G}_{\mathrm{j}}\boldsymbol{v}_n \end{bmatrix}. \tag{A.3}$$

The solution vector $\boldsymbol{z}$ contains the new velocities and the Lagrange multipliers. The position update is simply $\boldsymbol{x}_{n+1} = \boldsymbol{x}_n + \Delta t \boldsymbol{v}_{n+1}$. For notational convenience, a factor Δt has been absorbed in the multipliers such that the constraint force reads $\boldsymbol{G}^T\boldsymbol{\lambda}/\Delta t$. The upper and lower limits, u and l, in Eq. (A.1), follow from the contact law, and from any joint and motor limits. Since the limits depend on the solution, this is a partially nonlinear complementarity problem. The temporary slack variables, w_l and w_u, are used only internally by the MCP solver. In the present paper the full MCP is solved with a hybrid direct-iterative split solver using the simulation engine AGX Dynamics [33]. The articulated machine and the contact normal forces between the machine and rocks are thus solved using a sparse direct block-pivot LDLT solver [34]. The rock pile contact network and the friction forces between the machine and the rocks are solved to lower precision using a projected Gauss-Seidel (PGS) solver [12]. To accelerate the PGS solver computations, parallel processing using spatial domain decomposition and warmstarting [35] is employed.

Expressions for the constraint functions and Jacobians can be found in [12]. These depend on the particle positions and are evaluated at every time-step, based on the present configuration of joints and contacts, computed by means of geometric collision detection.

The regularization and constraint stabilization terms are related to compliance and damping coefficients as follows

$$\begin{aligned} \boldsymbol{\Sigma}_{\mathrm{n}} &= \frac{4}{\Delta t^2}\frac{\varepsilon_{\mathrm{n}}}{1 + 4\frac{\tau_{\mathrm{n}}}{\Delta t}}\mathbf{1}_{N_c \times N_c}, \\ \boldsymbol{\Sigma}_{\mathrm{t}} &= \frac{\gamma_{\mathrm{t}}}{\Delta t}\mathbf{1}_{2N_c \times 2N_c}, \\ \boldsymbol{\Sigma}_{\mathrm{r}} &= \frac{\gamma_{\mathrm{r}}}{\Delta t}\mathbf{1}_{3N_c \times 3N_c}, \\ \boldsymbol{\Upsilon}_{\mathrm{n}} &= \frac{1}{1 + 4\frac{\tau_{\mathrm{n}}}{\Delta t}}\mathbf{1}_{N_c \times N_c}, \end{aligned} \tag{A.4}$$

where $\varepsilon_{\mathrm{n}} = e_{\mathrm{H}}/k_{\mathrm{n}}$, $\gamma_{\mathrm{n}}^{-1} = k_{\mathrm{n}} c / e_{\mathrm{H}}^2$ and $\tau_{\mathrm{n}} = \max(n_{\mathrm{s}}\Delta t, \varepsilon_{\mathrm{n}}/\gamma_{\mathrm{n}})$, with elastic stiffness coefficient k_{n} and viscosity c. For the Hertz-Mindlin contact law, $e_{\mathrm{H}} = 5/4$, $k_{\mathrm{n}} = e_{\mathrm{H}} E \sqrt{r^*}/3(1-\nu^2)$ where $r^* = (r_a + r_b)/r_a r_b$ is the effective radius, E is the Young's modulus and ν is the Poisson ratio. For small relative contact velocities the normal force approximates $\boldsymbol{G}_{\mathrm{n}}^{(n)\mathrm{T}} \boldsymbol{\lambda}_{\mathrm{n}}^{(n)}/\Delta t \approx \varepsilon_{\mathrm{n}}^{-1} \boldsymbol{G}_{\mathrm{n}}^{(n)\mathrm{T}} \boldsymbol{g}_{\mathrm{n}}^{(n)} = \pm k_{\mathrm{n}} \left[\rho^{2e_{\mathrm{H}}-1} + c\rho^{2(e_{\mathrm{H}}-1)}\dot{\rho}\right] \boldsymbol{n}$, which is precisely the Hertz-Mindlin law in Eq. (9).

Collisions are separated into resting contacts and impacts using an impact threshold velocity v_{imp}. If the relative contact velocity is smaller than this value the contacts are modelled as described above. In case of impacts we apply the Newton impact law, $\boldsymbol{G}_{\mathrm{n}} \boldsymbol{v}^+ = -e \boldsymbol{G}_{\mathrm{n}} \boldsymbol{v}^-$ with restitution coefficient e, while preserving all other constraints in the system on the velocity level, $\boldsymbol{G}\boldsymbol{v}^+ = 0$. This is carried out in an impact stage solve, prior to the main solve for the constrained equations of motions (1)-(3). With this division, the restitution coefficient become the key parameter for modelling the dissipative part of the normal force. For the resting contacts we can simply enforce numerical stability using $\tau_{\mathrm{n}} = 4.5\Delta t$ with little consequence of the artificial damping [36]. In the limit of small time-steps, the physical viscous damping may be used by setting $\tau_{\mathrm{n}} = 5c_{\mathrm{d}}/4$ and not applying Newton's impact law.

Choosing time-step and solver iterations

For a given error tolerance ϵ in a NDEM simulation, the time-step should be chosen [37]

$$\Delta t \lesssim \min(\epsilon d/v_{\mathrm{n}}, \sqrt{2\epsilon d/\dot{v}_{\mathrm{n}}}) \qquad \text{(A.5)}$$

where v_{n} is the normal contact velocity and $\dot{v}_{\mathrm{n}}$ is the largest potential acceleration that can occur from the forces acting on a particle. In a dense packing the potential acceleration can be estimated by $\dot{v}_{\mathrm{n}} \sim \sigma A_{\mathrm{p}}/m_{\mathrm{p}}$, with particle cross-section $A_{\mathrm{p}} = \pi d^2/4$, mass m_{p} and the characteristic stress σ that may be estimated from known external loads. In the absence of external loads, the potential acceleration coincides with the gravity acceleration.

The number of projected Gauss-Seidel iterations has been found to satisfy the following relation [37]

$$N_{\mathrm{it}} \gtrsim 0.1 n/\epsilon \qquad \text{(A.6)}$$

where n is the length of the contact network (number of particles) in the direction of the dominant stress.

Two examples are considered next. Assume an error tolerance of $\epsilon = 0.01$ and consider a quasi-static system ($v_{\mathrm{n}} \approx 0$) with smallest particle diameter $d_{\mathrm{p}} = 0.01$ m, mass $m_{\mathrm{p}} = 0.001$ kg confined in a cubic container with side length $L = 1.0$ m and wall pressure σ. For a pressure of $\sigma = 1.0$ kPa the acceleration become $a = 78$ m/s^2 and the time-step limits $\Delta t \lesssim 1$ ms. For the larger pressure $\sigma = 100$ kPa we get $a = 7800$ m/s^2 and $\Delta t \lesssim 0.1$ ms. Since the side-length is $n \sim 100$ particle diameters, the number of iterations become $N_{\mathrm{it}} \gtrsim 1000$.

Appendix B. Particle scaling

The use of large pseudo-particles instead of true particle sizes is necessary for manageable number of particles and computational time. With a scale invariant numerical model, the particle sizes can be modified without affecting the bulk properties and without the need to identify a new set of simulation parameters.

We verified scale invariance through the same approach as Obermayr et al. [38]. All geometric quantities were scaled by a factor $\alpha = 0.5$, i.e. particle diameter and relative positions, as well as container and cone penetrometer dimensions. The penetration and compression rates were kept the same, preserving the inertial number. All model parameters are invariant by construction.

For an arbitrarily chosen numerical soil, we compared the original with the scaled models, as presented in Figure B.1 for the triaxial tests. Similarly, Figure B.2 shows the same comparison for the cone penetrometer test. Since the maximum penetration depth, h_{max}, differed between models, we defined the normalized quantity h/h_{max}, where h is the penetration depth. It was observed that the measured stresses were independent of particle size, up to a few percent. The tip resistances differed only with what was considered noise due to few cone-particle contacts.

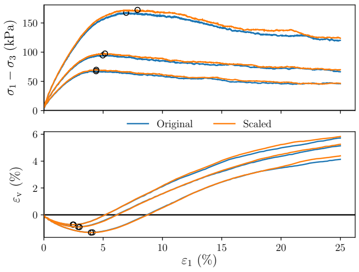

Figure B.1: Deviator stress and volumetric strain versus axial strain for simulated triaxial tests of the original and scaled models. The three confinement pressures are the standard 30, 50 and 100 kPa.

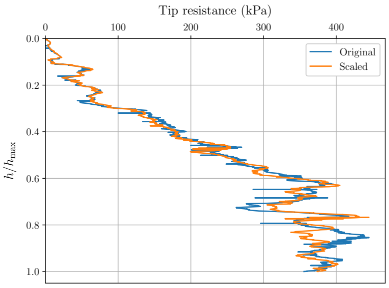

Figure B.2: Tip resistance versus normalized penetration depth for simulated cone penetrometer tests of the original and scaled models.

References

[1] R. Raper, Agricultural traffic impacts on soil, Journal of Terramechanics 42 (2005) 259 – 280. Assessing the Impacts of Military Vehicular Traffic on Natural Areas.

[2] M. Cambi, G. Certini, F. Neri, E. Marchi, The impact of heavy traffic on forest soils: A review, Forest Ecology and Management 338 (2015) 124–138.

[3] T. Pöschel, T. Schwager, Computational Granular Dynamics, Models and Algorithms, Springer-Verlag, 2005.

[4] B. Andreotti, Y. Forterre, O. Pouliquen, Granular Media: Between Fluid and Solid, 1st edition, Cambridge University Press, 2013.

[5] Y. T. Feng, D. R. J. Owen, Discrete element modelling of large scale particle systems—i: exact scaling laws, Computational Particle Mechanics 1 (2014) 159–168.

[6] S. Taheri, C. Sandu, S. Taheri, E. Pinto, D. Gorsich, A technical survey on terramechanics models for tire–terrain interaction used in modeling and simulation of wheeled vehicles, Journal of Terramechanics 57 (2015) 1 – 22.

[7] W. Smith, D. Melanz, C. Senatore, K. Iagnemma, H. Peng, Comparison of discrete element method and traditional modeling methods for steady-state wheel-terrain interaction of small vehicles, Journal of Terramechanics 56 (2014) 61 – 75.

[8] A. Recuero, R. Serban, B. Peterson, H. Sugiyama, P. Jayakumar, D. Negrut, A high-fidelity approach for vehicle mobility simulation: Nonlinear finite element tires operating on granular material, Journal of Terramechanics 72 (2017) 39–54.

[9] C. Coetzee, Review: Calibration of the discrete element method, Powder Technology 310 (2017) 104–142.

[10] M. Obermayr, et al., A discrete element model and its experimental validation for the prediction of draft forces in cohesive soil., Journal of Terramechanics 53 (2014) 93–104.

[11] C. Lacoursière, Regularized, stabilized, variational methods for multibodies, in: D. F. Peter Bunus, C. Führer (Eds.), The 48th Scandinavian Conference on Simulation and Modeling (SIMS 2007), 30-31 October, 2007, Göteborg (Särö), Sweden, Linköping University Electronic Press, 2007, pp. 40–48.

[12] M. Servin, D. Wang, C. Lacoursière, K. Bodin, Examining the smooth and nonsmooth discrete element approach to granular matter, Int. J. Numer. Meth. Engng. 97 (2014) 878–902.

[13] V. Acary, B. Brogliato, Numerical Methods for Nonsmooth Dynamical Systems: Applications in Mechanics and Electronics, Springer Verlag, 2008. URL: `http://hal.inria.fr/inria-00423530`.

[14] F. Radjai, F. Dubois, Discrete-element modeling of granular materials, Wiley-Iste, 2011.

[15] K. G. Murty, Linear Complementarity, Linear and Nonlinear Programming, Helderman-Verlag, Heidelberg, 1988.

[16] K. L. Johnson, Contact mechanics, Cambridge University Press, 1985.

[17] N. Estrada, E. Azéma, F. Radjai, A. Taboada, Identification of rolling resistance as a shape parameter in sheared granular media, Phys. Rev. E 84 (2011) 011306.

[18] J. Y. Wong, Terramechanics and Off-Road Vehicle Engineering, 2nd ed., John Wiley & Sons, 2009.

[19] M. Saarilahti, Soil interaction model. Project deliverable D2 (Work package no. 1) of the Development of a protocol for ecoefficient wood harvesting on sensitive sites (ecowood). EU 5th framework project (Quality of life and management of living resources), Contract No. QLK5-1999-00991 (1999–2002) (2002).

[20] B. M. Das, K. Sobhan, Principles of geotechnical engineering, Cengage learning, 2013.

[21] J. L. Perez, C. Kwok, C. O'Sullivan, X. Huang, K. Hanley, Assessing the quasi-static conditions for shearing in granular media within the critical state soil mechanics framework, Soils and Foundations 56 (2016) 152 – 159.

[22] J. Butlanska, M. Arroyo, A. Gens, Size effects on a virtual calibration chamber, Numerical Methods in Geotechnical Engineering: NUMGE (2010) 225–230.

[23] J. Butlanska, M. Arroyo, A. Gens, Virtual calibration chamber cpt on ticino sand, in: 2nd International Symposium on Cone Penetration Testing, Huntington Beach, CA, USA, 2010.

[24] N. Estrada, A. Taboada, F. Radjaï, Shear strength and force transmission in granular media with rolling resistance, Phys. Rev. E 78 (2008) 021301.

[25] R. Wismer, H. Luth, Off-road traction prediction for wheeled vehicles, Transactions of the ASAE 17 (1974) 8–0010.

[26] T. Anttila, Metsämaan raiteistumisen ennustaminen WES-menetelmää käyttäen. Publications 17. 53 p, Technical Report, University of Helsinki, Department of forest resource management, 1998.

[27] M. Saarilahti, Evaluation of the wes-method in assessing the trafficability of terrain and the mobility of forest tractors–part 2: Comparison of the different wes-models. soil interaction model, Soil interaction model, Appendix Report 3 (2002) 1–28.

[28] A. Pirnazarov, M. Wijekoon, U. Sellgren, B. Löfgren, K. Andersson, Modeling of the bearing capacity of nordic forest soil, in: Proceedings of the 12th European Regional Conference of the International Society for Terrain-Vehicle Systems, Pretoria, South Africa, 2012, pp. 24–27.

[29] A. T. Abebe, T. Tanaka, M. Yamazaki, Soil compaction by multiple passes of a rigid wheel relevant for optimization of traffic, Journal of Terramechanics 26 (1989) 139–148.

[30] D. Potyondy, P. Cundall, A bonded-particle model for rock, International Journal of Rock Mechanics and Mining Sciences 41 (2004) 1329 – 1364. Rock Mechanics Results from the Underground Research Laboratory, Canada.

[31] S. C. Thakur, J. P. Morrissey, J. Sun, J. F. Chen, J. Y. Ooi, Micromechanical analysis of cohesive granular materials using the discrete element method with an adhesive elasto-plastic contact model, Granular Matter 16 (2014) 383–400.

[32] C. Lacoursiére, Regularized, stabilized, variational methods for multibodies, The 48th Scandinavian conference on simulation and modeling (SIMS 2007), Göteborg, 30–31 (2007) 40–48.

[33] Algoryx Simulations, AGX dynamics, 2019. URL: `https://www.algoryx.se/products/agx-dynamics/`.

[34] C. Lacoursiére, M. Linde, O. Sabelström, Direct sparse factorization of blocked saddle point matrices, Para 2010: State of the Art in Scientific and Parallel Computing, Reykjavik, June 6-9 (2010).

[35] D. Wang, et al., Warm starting the projected gauss-seidel algorithm for granular matter simulation., Computational Particle Mechanics. 3 (2016) 43–52.

[36] D. Wang, M. Servin, T. Berglund, K.-O. Mickelsson, S. Rönnbäck, Parametrization and validation of a nonsmooth discrete element method for simulating flows of iron ore green pellets, Powder Technology 283 (2015) 475 – 487.

[37] M. Servin, D. Wang, C. Lacoursière, K. Bodin, Examining the smooth and nonsmooth discrete element approaches to granular matter, Journal for Numerical Methods in Engineering 97 (2014) 878–902.

[38] M. Obermayr, C. Vrettos, P. Eberhard, A discrete element model for cohesive soil, in: Proceedings of the international conference on particle-based methods–particles, 2013.